

Synergistically Improving the Stability and Operating Potential of Organic Cathodes for Sodium-Ion Battery

Shruti Suriyakumar⁺^[a], Aniruddha Mazumder⁺^[b], Patoju Sai Dilip,^[b] Mahesh Hariharan,^{*[b]} and Manikoth M. Shajumon^{*[a]}

Establishing a sustainable energy solution is one of the most important issues in achieving a greener community. Given the geographically limited cobalt resources, the rising concerns about the growth of electric vehicle sectors driven by lithium-ion batteries consisting of cobalt-based cathodes have pushed the research community to probe alternate avenues. In this endeavor, employing organic electrodes can open the road to green and sustainable batteries. Among many new emerging candidates, polyimides are still being considered as cathode candidates owing to their tunability. This work envisaged tailoring the reduction potential and enhancing the cycling stability of a perylene polyimide-based organic cathode

through a dual modification strategy. The influence of the twist induced by chlorine functionality at the bay position of perylene diimide and the role of the linker is systematically summarized. The correlation between the reduction potentials and the electron-withdrawing ability of the four-chlorine bay-substituent was supported by HOMO-LUMO energy levels and orbital iso-surface studies of the monomers. The accompanying thiourea linker group has significantly increased the cycling stability for 200 cycles at 1 A g^{-1} current density. This approach can be expanded to other organic battery chemistries for significantly enhanced electrochemical performance.

Introduction

Rechargeable batteries have found a special niche in numerous applications ranging from powering small electronic gadgets to grid storage applications.^[1,2] Among the four types of well-established rechargeable batteries, namely lithium-ion batteries (LIBs), lead (Pb)-acid, nickel-metal hydride (Ni–MH), and nickel-cadmium (Ni–Cd) batteries currently available, Pb-acid batteries have the largest market share.^[3] Lithium-ion batteries are also penetrating the electric vehicle market owing to their high energy density.^[4] The first use of intercalation chemistry to drive reversible electrochemical reactions dates to the 1990s wherein Sony announced their rechargeable cell composed of layered LiCoO_2 cathode and carbonaceous anode.^[5] With the expansion of the demand and applications, the price of lithium and cobalt resources is increasing.^[6] There are also concerns about the limited availability of lithium sources, and as a consequence, the pursuit of alternate chemistry has risen

considerably. It is also worth mentioning that there is a quest for alternate alkali earth metals for ion battery applications in particular. Though the research on sodium-ion chemistry began alongside Li-ion, the commercialization prospects were left scarcely pondered due to the dominance of the Li-ion market. It is, however, time to venture “beyond Li-ion” by shifting to sodium-ion batteries (SIB) and potassium-ion batteries (KIB) with similar chemistry.^[7] In general, oxides made of layered, spinel and olivine structures, polyanionic compounds are considered active materials in cathodes. Each of these materials has its own merits and demerits regarding its ion intercalation potential, theoretical capacity, and interfacial property with non-aqueous electrolytes. With a projected humongous rise in the electrification of vehicles, issues pertaining to the disposal and treatment of spent rechargeable batteries containing heavy metal elements, including nickel (Ni), cobalt (Co), and lead (Pb) are increasing. These metals are hazardous to human health and the environment if disposed of inappropriately.^[8] Owing to such environmental concerns, the need for sustainable green energy is becoming predominant, which calls for a shift from inorganic to organic electrode materials.^[9]

Organic materials are diverse by virtue of the possibility of functionalization. Such vast diversity is achieved by altering the functional groups and varying the position at which the functional group bonds with the parent organic molecule.^[10,11] The other features of organic materials that make them better than their inorganic counterpart include their low cost, lightweight, improved flexibility and resource renewability.^[12,13] Carbonyl compounds were the first of their kind to be employed as an organic cathode in a lithium battery. Though reported in 1969,^[14] the next groundbreaking results came more than a decade later, which reported the use of doped

[a] Dr. S. Suriyakumar,⁺ Prof. M. M. Shajumon
School of Physics

Indian Institute of Science Education and Research Thiruvananthapuram
Maruthamala PO, Vithura
Thiruvananthapuram, Kerala 695551 (India)
E-mail: shajju@iisertvm.ac.in

[b] A. Mazumder,⁺ P. S. Dilip, Prof. M. Hariharan
School of Chemistry

Indian Institute of Science Education and Research Thiruvananthapuram
Maruthamala PO, Vithura
Thiruvananthapuram, Kerala 695551 (India)
E-mail: mahesh@iisertvm.ac.in

[†] These authors contributed equally to this work.

 Supporting information for this article is available on the WWW under
<https://doi.org/10.1002/batt.202300111>

 An invited contribution to a Special Collection on Organic Batteries

polyacetylene as cathode material. In the process of finding an active organic electrode material, the electron affinity and the ability of different types of organic compounds to react reversibly with the alkali metal has been probed by numerous researchers.^[15] In one such research venture, Tobishima and their group studied 17 different organic compounds for application as electrode active material. This led to the first report of using 2,4,7-trinitro-9-fluorenone, a nitrile compound, as active material. It is also worth mentioning that research on the use of organic materials for other energy storage devices *viz* supercapacitors, hybrid capacitors, dual-ion and redox flow batteries, was also explored.^[16–23] When one looks for strategies to identify electrode materials, it is essential to distinguish between the requisites for the functioning of a cathode and anode. Upon functionalization, the functional groups alter the HOMO and LUMO energy levels of the parent organic molecule. Upon systematically evaluating the figure of merits of the organic electrode materials such as conductivity, energy density, power density, cost and stability, our group has been inclined towards the application of polyimides as organic electrode material. In particular, perylene tetracarboxylic dianhydride (PTCDA)-based polyimide cathode material derived by the polymerization approach poses properties such as the relative insolubility of electrode materials in the electrolytes upon cycling and the high structural stability of polyimide. These attributes make them potential alternative redox-active electrode materials for realizing sustainable and green electrochemical metal-ion batteries. Prominent examples of tailoring of these materials include the preparation of composites with rGO or CNT,^[24–27] impregnation or deposition of active material on carbon cloth,^[28,29] and adding large functional groups to the perylene diimide (PDI) skeleton.^[30,31] We reported how the dihedral angles in PDI could affect the shape of the discharge curve. It was observed that PDI with one and two Br displays two discharge plateaus, whereas PDI with three and four Br

shows one discharge plateau.^[30] Our approach differentiates from the prior art in such a way that we incorporate modifications that aid dual benefits. Confronted with interesting experimental evidence, a detailed study on the influence of chlorine substitution and linker group modification is thoroughly investigated in this work.

Results and Discussion

To begin with, since polymerization of perylenediimide derivatives is proposed as an able method to avoid electrode dissolution, polyimides have been synthesized with a urea linker. The synthesized samples were characterized by FTIR (Figure S1), CHNS and ¹³C solid-state MAS NMR techniques (Refer to Section 2: Results in Supporting Information). Further, they are proven to be thermally more stable than PTCDA.^[32] Generally, to tune the HOMO-LUMO of the compound, halides are attached to the bay position of the polyimides. Our group has earlier ventured into introducing various moieties on the polyimides. The structure and voltage profile correlation were studied by analyzing the influence of core twists induced by the electron-withdrawing groups. We begin with a theoretical calculation on the energy of the halides introduced in the bay position of the PTCDA. Of the halides, F, Cl and Br, it is found that PDI with Br substitution has the most stable configuration. However, considering the fact that Br has already been explored by our group and is more toxic compared to the other halides, we have opted for Cl substitution (Figure S2). Electrodes composed of polyimides synthesized using urea linker with and without chlorine substitution (PDI(U)-Cl₄ and PDI(U), respectively) were prepared, and half cells with sodium metal were fabricated. The cyclic voltammetry (CV) profile of both electrodes is presented in Figure 1(a). It is inferred that the CV of PDI(U) shows a pair of reduction peaks around 1.7 and 2.2 V

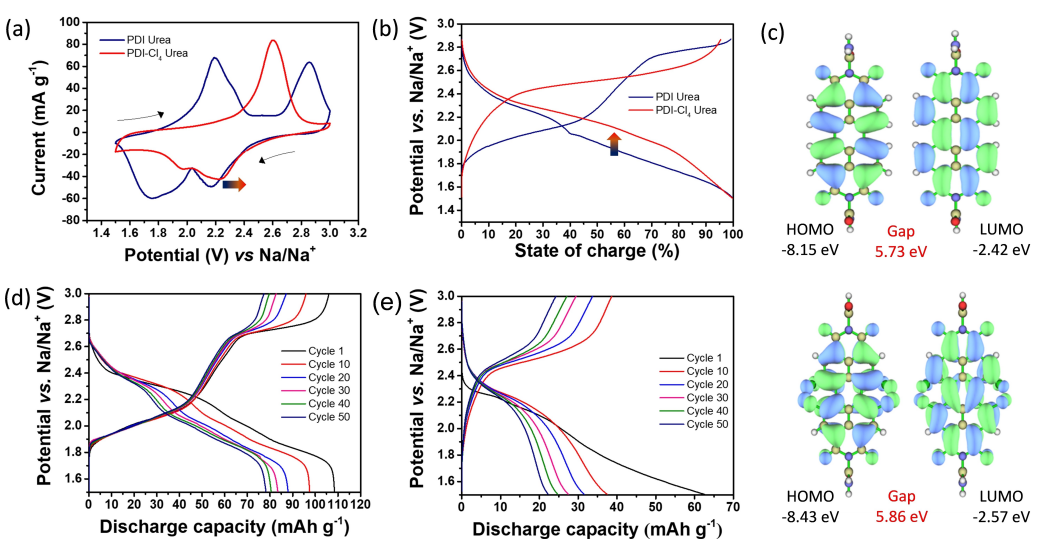


Figure 1. a) CV curves scanned at 0.2 mV s⁻¹ at the third cycle. b) Superimposition of the state of charge vs. potential curves for PDI(U) and PDI(U)-Cl₄. c) HOMO-LUMO iso-surfaces of PDI(U) (Top) and PDI(U)-Cl₄ (Bottom) monomers computed at ωB97XD/6-311+G(d,p) level of theory. Cycling profile of d) PDI(U) and e) PDI(U)-Cl₄ at 100 mA g⁻¹ current density at room temperature.

and a pair of oxidation peaks around 2.2 and 2.9 V. Interestingly and to our surprise, for PDI(U)-Cl₄ half-cell, we observe a single oxidation peak at 2.6 V and two reduction peaks at 1.9 and 2.3 V. We corroborated the influence on the charge-discharge profile due to reduction and oxidation peak positions. Figure 1(b) shows the normalised state of the charge vs potential curves wherein the PDI(U)-Cl₄ has an altered cycling profile with increased discharge potential. To summarise, introducing the electron-withdrawing group results in decreased electron density at the sodiation sites leading to an increase in the reduction potential. In the planar geometry, two sets of relatively sharp redox peaks are observed corresponding to the formation of radical anion and dianion, respectively. Interestingly, upon Cl substitution, in order to avoid electrostatic repulsions between the Cl substituents and the hydrogen atoms on opposite bay positions, the perylene ring stabilizes into a twisted geometry. We clearly understand that the high degree of delocalization of the perylene cores due to Cl substitution favours direct dianion formation, resulting in one broader peak in the cycling curve.

To establish a correlation between the reduction potentials and the electron-withdrawing ability of the four-chlorine bay-substituents, HOMO-LUMO energy levels and orbital iso-surfaces of the monomers PDI(U) and PDI(U)-Cl₄ were computationally evaluated (Figure 1c-Top and 1c-Bottom, respectively). LUMO energy levels are known to directly correspond to the reduction potentials of the molecules and were calculated for the monomers in their gaseous phase using the ω B97XD/6-311+G(d,p) level of theory.^[33] The LUMO energy value obtained for PDI(U) was -2.42 eV, whereas PDI(U)-Cl₄ exhibited a significantly lower LUMO energy value of -2.57 eV (Figure 1c). The first reduction potentials observed in the cyclic voltammetric plots (Figure 1a) show a linear relationship with the calculated LUMO energy values, thus, correlating the increase in the reduction potentials to the electron-withdraw-

ing ability of the chlorine substituents in PDI(U)-Cl₄.^[30] This remarkable concurrence between the experimental and theoretical results demonstrates the flexibility that organic molecules offer in tuning the materials for desired cathode properties. Further, changes in the dihedral angles of a neutral PDI derivative definitely have an effect on the relative energies of its reduced forms (radical anion and dianion). A single redox peak meant a complete preference for the formation of the dianion over the radical anion. Our group has carried out a detailed theoretical study investigating the role of twist.^[30] This was evident from the greater ΔG values for dianion. Further, the work experimentally supports the concept by evidencing the two-step discharge in the planar PDI with sulfur ($\sim 6^\circ$) at the 4 bay positions. Figure 1(d and e) shows the cycling profiles of the two electrodes cycled at 100 mA g⁻¹ current density at room temperature. The decrease in initial discharge capacity might be attributed to the increased density of the PDI(U)-Cl₄ due to the heavy Cl atom substitution. Despite this significant shift in the reduction potential, the cycling stability is still under threat owing to the solubility of the organic electrodes in the solvent. This issue has been strategically addressed by introducing thiourea-motifs as linkers during polyimide preparation.

Interestingly, the stability of all the organic electrodes can be observed through the visual solubility test,^[34,35] wherein equal amounts of these polyimides are added to the solvent, and the change in color of the liquid with time by the dissolution is noted. The degree of color change is used to qualitatively estimate the extent of solubility. It is found from Figure 2(a) that, of all the three samples, the dissolution-induced color change is the least in PDI(T)-Cl₄. Since the solubility factor is paramount in influencing cell performance, we will further probe the theoretical and electrochemical properties of PDI(U)-Cl₄ and PDI(T)-Cl₄. In other words, the effect of linker modification on the kinetics will be thoroughly investigated and discussed in the following section. Henceforth,

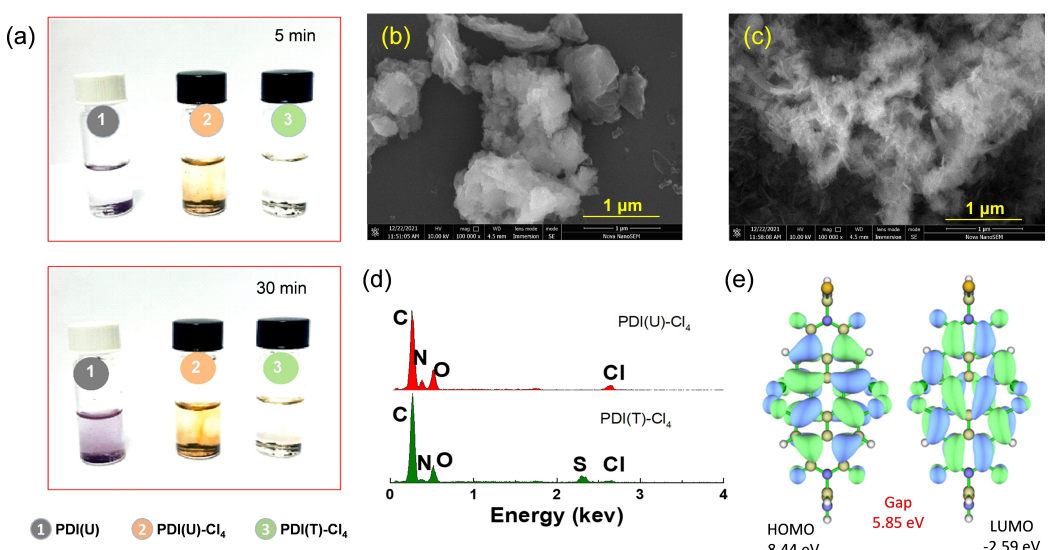


Figure 2. a) Visual dissolution test of the organic materials. SEM images of b) PDI(U)-Cl₄ and c) PDI(T)-Cl₄. d) EDX spectra of PDI(U)-Cl₄ (Top) and PDI(T)-Cl₄ (Bottom). e) HOMO-LUMO iso-surfaces of PDI(T)-Cl₄ monomer computed at ω B97XD/6-311+G(d,p) level of theory.

PDI(U)-Cl₄ (urea) to PDI(T)-Cl₄ (thiourea) will be considered for the study. The SEM images of the PDI(U)-Cl₄ and PDI(T)-Cl₄ appear strikingly different, with the latter having a more flared structure (Figure 2b and c). The EDX spectra in Figure 2(d) aid in identifying the sulfur from the thiourea linker in the PDI(T)-Cl₄. The role of linker modification from PDI(U)-Cl₄ (urea) to PDI(T)-Cl₄ (thiourea) in altering the reduction potential of these materials was theoretically analyzed by calculating the HOMO-LUMO energy levels and iso-surfaces for the monomers in their gaseous phase using ωB97XD/6-311+G(d,p) level of theory (Figure 2e). Significant stabilization of the LUMO energy level was not observed while going from PDI(U)-Cl₄ (-2.57 eV) to PDI(T)-Cl₄ (-2.59 eV). Therefore, it is expected that the influence of the thiourea linker on the reduction potentials of the cathode materials is minimum or negligible.

We observe a similar trend upon extending the HOMO-LUMO energy level and iso-surface calculations to dimers of PDI(U), PDI(U)-Cl₄ and PDI(T)-Cl₄, respectively (Figure S3). The electron-withdrawing chlorine substituted dimers exhibited considerable stabilization of the LUMO energy level (-2.64 eV for PDI(U)-Cl₄ and -2.62 eV for PDI(T)-Cl₄), compared to the unsubstituted PDI(U) dimer (-2.45 eV). The electron density is distributed on one fragment (monomer) in HOMO and on the other fragment in LUMO for both PDI(U) and PDI(U)-Cl₄ dimers. Interestingly, the electron density distribution for PDI(T)-Cl₄ was different and was evenly spread over both the fragments in LUMO (Figure S3), most probably due to the extended conjugation through the thiourea linker S atoms. As the number of monomers (*n*) increases in the polymer, the stabilization of the LUMO energy level could be more pronounced in the case of PDI(U)-Cl₄ and PDI(T)-Cl₄, thereby offering a higher reduction potential compared to the PDI(U) polymer. Apart from modifying the HOMO-LUMO energy levels of the molecules, the chlorine substituents also introduce a twist in the perylene core, which directly affects the relative

energies of perylene's reduced forms (radical anion and dianion). In order to avoid chlorine-chlorine electrostatic repulsions, the perylene ring adopts a twisted geometry. The different dihedral angles between the naphthalene subunits (core-twist) and between the linker and perylene ring for the three monomers are shown in Figure S4. The perylene core was found to be nearly planar with a core twist of 0.04° in PDI(U), 33.30° in PDI(U)-Cl₄ and 33.47° in PDI(T)-Cl₄. The change in the shape of the charge-discharge profile from the double plateau to the single plateau is presumably due to the core twist induced as a result of chlorine substitution. The O/S-C-N-C dihedral angle (between linker and perylene ring) was found to be 84.03° in PDI(U), 86.94° in PDI(U)-Cl₄ and 88.65° in PDI(T)-Cl₄. The large dihedral angles between the linker and perylene ring indicated that the carbonyl/thiocarbonyl groups in the linker were non-planar and non-conjugated with the perylene units.^[30]

To further have a deep understanding of the sodiation mechanism, the energies of the possible products during the sodiation process were calculated by density functional theory (DFT) for all the monomers.^[36] The sodiated monomer structures were optimized, and single-point energy calculations were performed on the optimized structures at ωB97XD/6-311+G(d,p) level of theory (Figure S5). Consistent with our experimental results, it was observed that the Na ions prefer to bind more selectively with S atoms instead of O atoms for PDI(T)-Cl₄ (Figure S5c), in the case of both mono-sodiation and di-sodiation.^[37] These interaction studies verified the role of S atoms in PDI(T)-Cl₄ to modify the sodiation site and increase the overall stability and robustness of the cathode material, as observed from the galvanostatic cyclic measurements and visible solubility studies. To distinguish the kinetics of the electrodes, *b* values estimation through CV by scanning at various sweep rates was performed. Using Randles Sevcik equation, *b* values were deduced through peak current

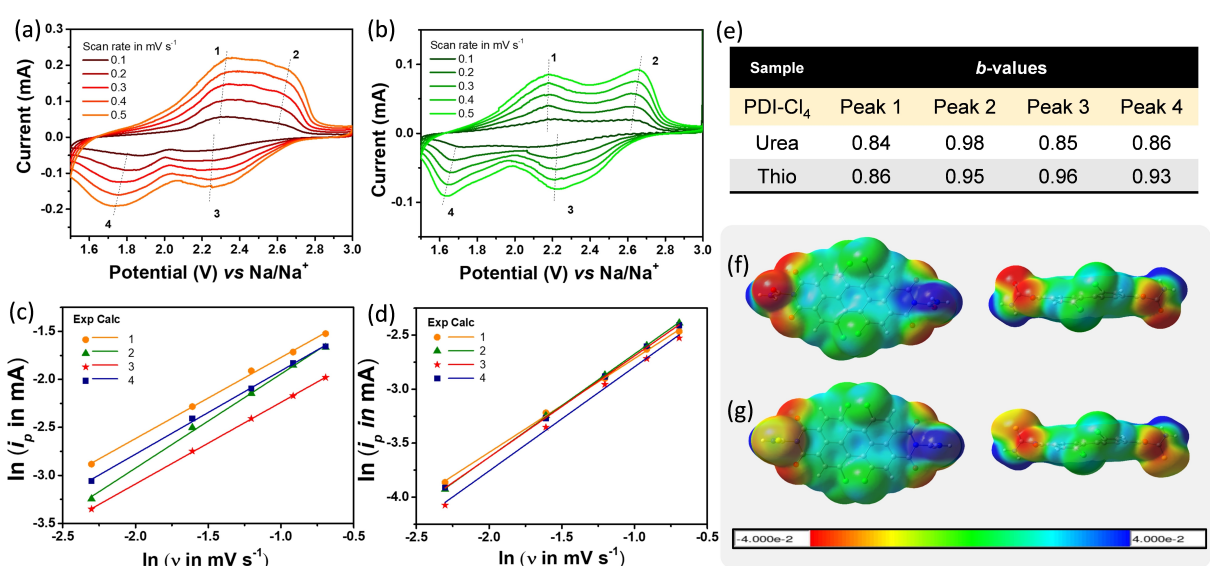


Figure 3. CV curves at different scan rates recorded for a) PDI(U)-Cl₄ and b) PDI(T)-Cl₄. Relationship of peak current and scan rate plotted for c) PDI(U)-Cl₄ and d) PDI(T)-Cl₄, respectively. e) *b* values estimated from the slopes of the fitted linear graphs. MESP plots of f) PDI(U)-Cl₄ and g) PDI(T)-Cl₄.

measurements at the two anodic (labelled 1&2) and cathodic (labelled 3&4) peak positions. It is evident from Figure 3(a and b) that the peak-to-peak separation increases with an increase in scan rate, which is also in direct correlation with the equation.^[38] From the slope of $\ln(I_p)$ vs. $\ln(v)$ plot (Figure 3c and d), the diffusion coefficient values are calculated and presented in Figure 3(e). It can be inferred that the PDI(T)-Cl₄ has a higher b than PDI(U)-Cl₄. This is attributed to the extended conjugation in the molecular structure, which results in a surface-dominated charge storage mechanism. Molecular electrostatic surface potential (MESP) maps were calculated to confirm the possible sodiation sites (O atoms and S atoms) in PDI(U)-Cl₄ and PDI(T)-Cl₄. Introducing electron-withdrawing groups like chlorine leads to decreased electron densities on the sodiation site and higher redox potentials in PDI systems. According to the MESP plot, C=S (thiourea linker) exhibited lower electron densities among the possible sodiation sites in PDI(T)-Cl₄ (Figure 3g), whereas C=O (urea linker) demonstrated higher electron densities in PDI(U)-Cl₄ (Figure 3f). Figure 4(a) shows the cycling profile of the PDI(T)-Cl₄ at 100 mA g⁻¹. The half-cell shows a remarkably stable discharge capacity compared to the other PDI counterparts. Figure 4(b) shows the increment in Coulombic efficiency with cycle number, the efficiency of 98% at the 50th cycle. The schematic representation of replacement of oxygen with sulfur at the linker moiety in PDI(T)-Cl₄ is depicted in Figure 4(c). The rate capability studies depicted in Figure 4(d) show the dominance of the PDI(T)-Cl₄ at high current density. Though the PDI(U) contributed to a high capacity at low current rates, the capacity drops significantly at high currents. The theoretical capacity of these electrodes is calculated assuming a 2-electron transfer process and are shown in Table S1. It is observed that the

capacity retention of PDI(T)-Cl₄ is also appreciable. The cell delivers a discharge capacity of 63 mA h g⁻¹ when cycled back at 50 mA g⁻¹. The long cycling results (Figure 4e) of the three electrodes in half-cell configuration show that PDI(T)-Cl₄ outperforms the other electrodes. The low electron density of C=S in PDI(T)-Cl₄ (Figure 3g) contribute to the positive shift of the reduction potential when compared to PDI(U)-Cl₄.^[39] Further, the performance of the modified PDI(T)-Cl₄ cathode is compared with reports^[30,32,40-44] and presented in Table S2.

The theoretical findings were corroborated by the broad first reduction potentials observed in the differential capacity plots (Figure 5a) of PDI(U)-Cl₄ and PDI(T)-Cl₄. Though no marked difference is seen in the peak position, a peak broadening is observed in the case of PDI(T)-Cl₄. This can be ascribed to the extended conjugation resulting from the thiourea moiety incorporation. In our work, we have gone one step ahead and carried out EIS measurements at various state-of-charge to add more insights into the relationship between potential and sodium ion incorporation during the discharge process. The normalized discharge curve and the potentials at which impedance measurements were carried out are marked and presented in Figure 5(b). The dominance of Warburg is explicit at the high potential regions for PDI(U)-Cl₄ and PDI(T)-Cl₄. Compared to PDI(U)-Cl₄, PDI(T)-Cl₄ exhibits a drastic decrease in R_{ct} (Figure 5c). This is also in correlation with the MESP plots and diffusion coefficient studies. X-ray photoelectron spectroscopic (XPS) post-mortem studies were carried out to support our claim. The spectra of pristine and sodiated PDI(U)-Cl₄, and PDI(T)-Cl₄ were obtained and shown in Figure S6. The sodiated electrodes were carefully dismantled inside the glovebox and transferred into the XPS chamber with minimum air exposure. The sodiation of PDI(U)-Cl₄ is evidenced by a reduction in C=O

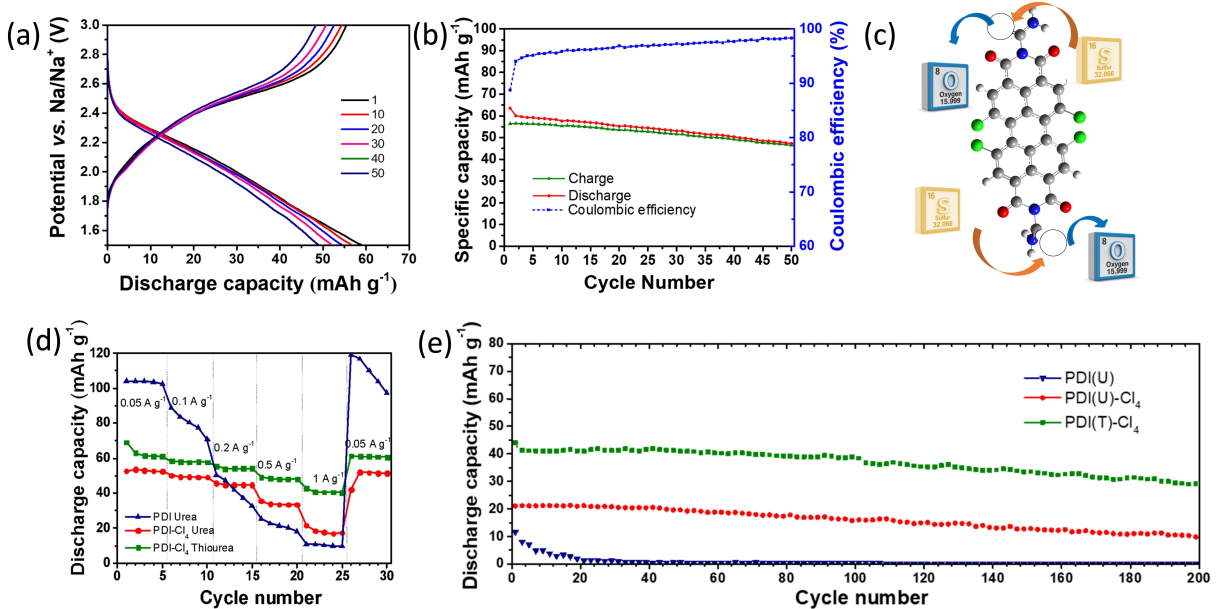


Figure 4. Electrochemical performance evaluation. Galvanostatic cycling studies of PDI(T)-Cl₄. a) cycling profile and b) cycle number vs. capacity plot for 50 cycles at 100 mA g⁻¹. c) Schematic representation of thio-linker incorporation to PDI. d) Rate capability and e) long cycling studies at 1 A g⁻¹ for the three electrodes.

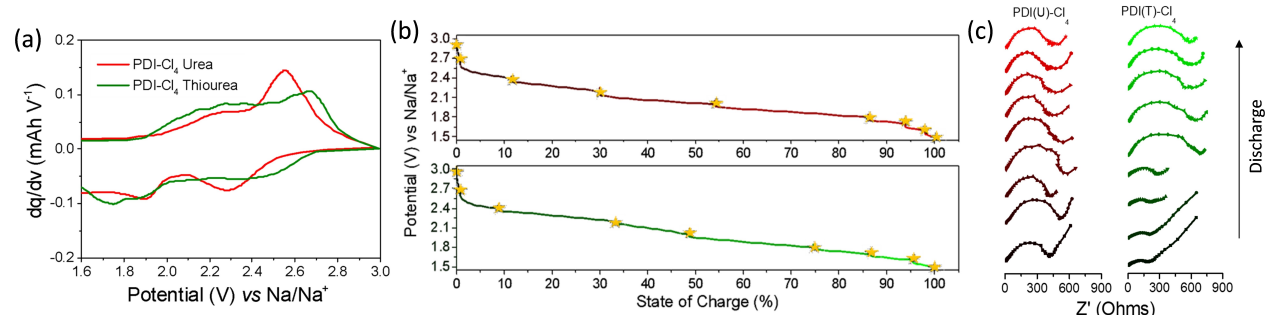


Figure 5. a) Differential capacity plots of cells cycled at 50 mA g⁻¹ in a voltage range between 1.5 and 3.0 V vs. Na⁺/Na⁺. b) Normalized discharge curves for PDI(U)-Cl₄ (red) and PDI(T)-Cl₄ (green) and c) EIS plots at different states of charge for PDI(U)-Cl₄ and PDI(T)-Cl₄.

bond and the appearance or increment of the peak corresponding to C—O/C—O—Na bond at 536.5 eV. On the contrary, there are no marked changes in the O 1s spectra of the PDI(T)-Cl₄ electrode. In close agreement with the MESP results, we notice the appearance of a new S 2p peak in the cycled cathode attributing to the formation of a metal-S-O bond.^[45] We hence propose a surface-controlled pseudo capacitive charge storage mechanism. The improvement of the cell performance of PDI(T)-Cl₄ can be attributed to the two parallel manipulations of the PDI skeleton. The electron-withdrawing chlorine addition enhances potential, and the thiourea linker synergistically improves the stability. This is, therefore, a versatile approach that can be extended to numerous other classes of potential organic electrodes.

Conclusion

Organic electrodes of diverse classes are blooming as sustainable alternatives to inorganic electrodes for alkali metal batteries. However, the associated challenges, including solubility, appreciable operating voltage and cycling performance, must be overcome. This work offers a dual modification approach to simultaneously tweak the reduction potential and address the solubility issues. The functional group-dependent change in reduction potential is substantiated with theoretical aids, including HOMO-LUMO calculations. Further, MESP plots are exploited to provide deeper insights into the contribution of thio-linkers in elevating the stability of organic electrodes in the electrolyte medium. The PDI(T)-Cl₄ electrode delivers a capacity of 37 mA h g⁻¹ even after 200 cycles at 1 A g⁻¹ current density. It is worth mentioning that cycling stability could be improved by incorporating thio-linkers without losing their favorable properties. This versatile approach can be applied to other organic electrode candidates for promising sustainable energy solutions.

Experimental Section

The synthesis procedures and material characterization are detailed in the Supporting Information. All chemicals were obtained from

commercial suppliers and used as received without further purification. All reactions were carried out in oven-dried glassware prior to use. Solvents were dried and distilled by standard laboratory purification techniques. Melting points were obtained using a capillary melting point apparatus. ¹H and ¹³C MAS NMR spectra were measured on a 500 MHz Bruker advance DPX and 500 MHz Bruker Neo Solid-state spectrometers, respectively. The internal standard used for ¹H and ¹³C NMR is tetramethylsilane (TMS).

Physico-chemical studies

SEM imaging and EDS analysis of the samples were studied using a Field-emission scanning electron microscope (Nova NANOSEM 450). The samples were dispersed in iso-propanol and drop coated onto a silicon wafer, and dried prior to imaging. Fourier transform infrared spectroscopy (FTIR) measurements of PDI(U), PDI(U)-Cl₄ and PDI(T)-Cl₄ were recorded on a Shimadzu IR Prestige-21 FTIR spectrometer as KBr pellets. X-ray photoelectron spectroscopic (XPS) measurements of PDI(U), PDI(U)-Cl₄ and PDI(T)-Cl₄ solid samples were performed using an ESCA Plus spectrometer (Omicron Nanotechnology Ltd, Germany). Mg K_α (1253.6 eV) was used as the X-ray source operating at 100 watts. General scans and core-level spectra were acquired with 1 eV and 50 eV pass energy, respectively. Spectral Background (Shirely) de-convolution was done by using CasaXPS software.^[46] For the visual solubility test, 5 mg of cathode active material was added to 2 mL of electrolyte solvent and the dissolution with time was noted.

Electrochemical studies

The organic electrode materials chosen for our study were prepared and characterised as detailed in Supporting Information. The electrochemical studies of these organic materials were performed by fabricating CR 2032-type coin cells. Briefly, the electrode slurry composed of 60% organic cathode material, 30% Super P carbon and 10% PVDF binder prepared with NMP as solvent was coated on stainless steel mesh and dried at 120 °C in a vacuum oven. Using a polished sodium metal anode, the organic cathode of 2–3 mg loading, the cell was assembled inside an argon-filled glove box. Glass fibre separator activated in a typical electrolyte composed of 1 M NaPF₆ in EC PC was used for the assembly. The cell was allowed to rest for 3 h post assembly and subjected to electrochemical tests (BioLogic VMP3, France). Being a cathode candidate, cyclic voltammetry at various sweep rates and cycling measurements at different current rates were carried out in the voltage window of 1.5–3 V vs. Na/Na⁺. dq/dV plots and log I vs. log v plots were deduced to get deeper insights into the kinetics and mechanism of charge storage in the organic electrodes. For the

potentiostatic electrochemical impedance measurements, a 10 mV sinusoidal AC perturbation voltage having a frequency in the range of 1 M kHz to 100 mHz was applied to the cell at different voltages congruent to various states of charge during discharge. The Nyquist plots were fit with the aid of the Z fit available in the EC lab module.

Computational analysis

All the calculations are carried out in Gaussian 16^[47] employing the ωB97XD functional and 6-311+G(d,p) basis set at the DFT level of theory in a vacuum unless stated otherwise. The frontier molecular orbitals (FMO) of PDI(U), PDI(U)-Cl₄ and PDI(T)-Cl₄ were obtained from the generated cube files of energy calculations, high-quality FMO isosurfaces were created using Multiwfn 3.8^[48] software. Geometry optimizations and single point energy (SPE) calculations were carried out using ωB97XD functional and 6-311+G(d,p) basis set at the DFT level of theory in Gaussian 16. Molecular electrostatic surface potential (MESP) maps were calculated for the optimized monomers of PDI(U), PDI(U)-Cl₄ and PDI(T)-Cl₄ in GaussView 5.0.8^[49] software.

Supporting Information

Additional references cited within the Supporting Information.^[50,51]

Acknowledgements

The authors acknowledge IISER Thiruvananthapuram for the financial and infrastructural support. We greatly acknowledge the support for high-performance computing time at the Padmanabha cluster at IISER Thiruvananthapuram, India. We greatly thank Dr. Ebin Sebastian for helping synthesise the cathode polyimides. S.S. gratefully acknowledges the financial support from the Science and Engineering Research Board, Department of Science & Technology, Govt. of India [PDF/2020/000209]. A.M. acknowledges IISER Thiruvananthapuram for financial assistance.

Conflict of Interest

The authors declare no conflict of interest.

Data Availability Statement

The data that support the findings of this study are available in the supplementary material of this article.

Keywords: cycling stability • MESP plots • organic batteries • perylene polyimides • sodium-ion batteries

- [1] M. S. Whittingham, *Science* **1976**, *192*, 1126.
- [2] M. R. Palacín, *Chem. Soc. Rev.* **2009**, *38*, 2565.
- [3] J. B. Goodenough, *J. Solid State Electrochem.* **2012**, *16*, 2019.

- [4] J. Dunn, M. Slattery, A. Kendall, H. Ambrose, S. Shen, *Environ. Sci. Technol.* **2021**, *55*, 5189.
- [5] M. S. Whittingham, *Chem. Rev.* **2004**, *104*, 4271.
- [6] G. A. Campbell, *Miner. Econ.* **2020**, *33*, 21.
- [7] K. Kubota, M. Dahbi, T. Hosaka, S. Kumakura, S. Komaba, *Chem. Rec.* **2018**, *18*, 459.
- [8] X. Zhang, L. Li, E. Fan, Q. Xue, Y. Bian, F. Wu, R. Chen, *Chem. Soc. Rev.* **2018**, *47*, 7239.
- [9] C. Fribe, A. Lex-Balducci, U. S. Schubert, *ChemSusChem* **2019**, *12*, 4093.
- [10] Z. Jin, Q. Cheng, A. M. Evans, J. Gray, R. Zhang, S. T. Bao, F. Wei, L. Venkataraman, Y. Yang, C. Nuckolls, *Chem. Sci.* **2022**, *13*, 3533.
- [11] J. Wang, H. Liu, C. Du, Y. Liu, B. Liu, H. Guan, S. Guan, Z. Sun, H. Yao, *Chem. Sci.* **2022**, *13*, 11614.
- [12] Z. Song, H. Zhou, *Energy Environ. Sci.* **2013**, *6*, 2280.
- [13] K. Qin, J. Huang, K. Holguin, C. Luo, *Energy Environ. Sci.* **2020**, *13*, 3950.
- [14] D. L. Williams, J. J. Byrne, J. S. Driscoll, *J. Electrochem. Soc.* **1969**, *116*, 2.
- [15] R. R. Kapaev, A. Zhugayevich, S. V. Ryazantsev, D. A. Aksyonov, D. Novichkov, P. I. Matveev, K. J. Stevenson, *Chem. Sci.* **2022**, *13*, 8161.
- [16] Y. Katsuyama, T. Takehi, S. Sakabe, M. Tanaka, M. Ishizawa, H. Abe, M. Watanabe, I. Honma, Y. Nakayasu, *Sci. Rep.* **2022**, *12*, 1.
- [17] J. Winsberg, T. Hagemann, T. Janoschka, M. D. Hager, U. S. Schubert, *Angew. Chem. Int. Ed.* **2017**, *56*, 686.
- [18] L. Fan, Q. Liu, Z. Xu, B. Lu, *ACS Energy Lett.* **2017**, *2*, 1614.
- [19] G. Vardhini, S. Suriyakumar, M. M. Shaijumon, *ACS Appl. Energ. Mater.* **2022**, *5*, 9595.
- [20] S. Park, I. Kristanto, G. Y. Jung, D. B. Ahn, K. Jeong, S. K. Kwak, S. Y. Lee, *Chem. Sci.* **2020**, *11*, 11692.
- [21] X. Zhang, X. Liu, H. Zhang, Z. Wang, Y. Zhang, G. Li, M. J. Li, G. He, *ACS Appl. Mater. Interfaces* **2022**, *14*, 8.
- [22] C. Wei, L. Tan, Y. Zhang, B. Xi, S. Xiong, J. Feng, *ACS Appl. Mater. Interfaces* **2022**, *14*, 2979.
- [23] Y. Liu, W. Luo, S. Lu, Z. Zhang, Z. Chao, J. Fan, *ACS Appl. Mater. Interfaces* **2022**, *14*, 53702.
- [24] X. Fan, F. Wang, X. Ji, R. Wang, T. Gao, S. Hou, J. Chen, T. Deng, X. Li, L. Chen, C. Luo, L. Wang, C. Wang, *Angew. Chem. Int. Ed.* **2018**, *130*, 7264.
- [25] H. Wu, K. Wang, Y. Meng, K. Lu, Z. Wei, *J. Mater. Chem. A* **2013**, *1*, 6366.
- [26] H. Lyu, P. Li, J. Liu, S. Mahurin, J. Chen, D. K. Hensley, G. M. Veith, Z. Guo, S. Dai, X. G. Sun, *ChemSusChem* **2018**, *11*, 763.
- [27] B. Chang, J. Ma, T. Jiang, L. Gao, Y. Li, M. Zhou, Y. Huang, S. Han, *RSC Adv.* **2020**, *10*, 8729.
- [28] G. Hernández, N. Casado, A. M. Zamarayeva, J. K. Duey, M. Armand, A. C. Arias, D. Mecerreyes, *ACS Appl. Energ. Mater.* **2018**, *1*, 7199.
- [29] P. Luo, Y. Xiao, J. Yang, C. Zuo, F. Xiong, C. Tang, G. Liu, W. Zhang, W. Tang, S. Wang, S. Dong, Q. An, *Chem. Eng. J.* **2022**, *433*, 133772.
- [30] H. Banda, D. Damien, K. Nagarajan, A. Raj, M. Hariharan, M. M. Shaijumon, *Adv. Energy Mater.* **2017**, *7*, 1701316.
- [31] M. Veerababu, R. Kothandaraman, *Electrochim. Acta* **2017**, *232*, 244.
- [32] H. Banda, D. Damien, K. Nagarajan, M. Hariharan, M. M. Shaijumon, *J. Mater. Chem. A* **2015**, *3*, 10453.
- [33] Z. Song, H. Zhan, Y. Zhou, *Angew. Chem. Int. Ed.* **2010**, *49*, 8444.
- [34] X. Wang, Z. Shang, A. Yang, Q. Zhang, F. Cheng, D. Jia, J. Chen, *Chem* **2019**, *5*, 364.
- [35] L. Cui, L. Zhou, K. Zhang, F. Xiong, S. Tan, M. Li, Q. An, Y. M. Kang, L. Mai, *Nano Energy* **2019**, *65*, 103902.
- [36] X. Gao, Y. Chen, C. Gu, J. Wen, X. Peng, J. Liu, Z. Zhang, Q. Zhang, Z. Liu, C. Wang, *J. Mater. Chem. A* **2020**, *8*, 19283.
- [37] B. Zhang, Y. Zhang, X. Yang, G. Li, S. Zhang, Y. Zhang, D. Yu, Z. Liu, G. He, *Chem. Mater.* **2020**, *32*, 10575.
- [38] N. N. Elgrishi, K. J. Rountree, B. D. McCarthy, E. S. Rountree, T. T. Eisenhart, J. L. Dempsey, *J. Chem. Educ.* **2018**, *95*, 197.
- [39] L. Liu, L. Miao, L. Li, F. Li, Y. Lu, Z. Shang, J. Chen, *J. Phys. Chem. Lett.* **2018**, *9*, 3573.
- [40] W. Deng, Y. Shen, J. Qian, Y. Cao, H. Yang, *ACS Appl. Mater. Interfaces* **2015**, *7*, 21095.
- [41] T. Huang, D. Lu, L. Ma, X. Xi, R. Liu, D. Wu, *Chem. Eng. J.* **2018**, *349*, 66.
- [42] C. N. Gannett, J. Kim, D. Tirtariyadi, P. J. Milner, H. D. Abruna, *Chem. Sci.* **2022**, *13*, 9191.
- [43] M. R. Raj, N. Kim, G. Lee, *Sustain. Energy Fuels* **2021**, *5*, 175.
- [44] M. Ruby Raj, R. V. Mangalaraja, D. Contreras, K. Varaprasad, M. V. Reddy, S. Adams, *ACS Appl. Energ. Mater.* **2020**, *3*, 240.
- [45] P. M. Shanthi, P. J. Hanumantha, K. Ramalinga, B. Gattu, M. K. Datta, P. N. Kumta, *J. Electrochem. Soc.* **2019**, *166*, A1827.
- [46] N. Fairley, V. Fernandez, M. Richard-Plouet, C. Guillot-Deudon, J. Walton, E. Smith, D. Flahaut, M. Greiner, M. Biesinger, S. Tougaard, D. Morgan, J. Baltrusaitis, *Appl. Surf. Sci. Adv.* **2021**, *5*, 100112.

- [47] M. J. Frisch, G. W. Trucks, H. B. Schlegel, G. E. Scuseria, M. A. Robb, J. R. Cheeseman, G. Scalmani, V. Barone, G. A. Petersson, H. Nakatsuji, X. Li, M. Caricato, A. V. Marenich, J. Bloino, B. G. Janesko, R. Gomperts, B. Mennucci, H. P. Hratchian, J. V. Ortiz, A. F. Izmaylov, J. L. Sonnenberg, D. Williams-Young, F. Ding, F. Lipparini, F. Egidi, J. Goings, B. Peng, A. Petrone, T. Henderson, D. Ranasinghe, V. G. Zakrzewski, J. Gao, N. Rega, G. Zheng, W. Liang, M. Hada, M. Ehara, K. Toyota, R. Fukuda, J. Hasegawa, M. Ishida, T. Nakajima, Y. Honda, O. Kitao, H. Nakai, T. Vreven, K. Throssell, J. A. Montgomery, Jr., J. E. Peralta, F. Ogliaro, M. J. Bearpark, J. J. Heyd, E. N. Brothers, K. N. Kudin, V. N. Staroverov, T. A. Keith, R. Kobayashi, J. Normand, K. Raghavachari, A. P. Rendell, J. C. Burant, S. S. Iyengar, J. Tomasi, M. Cossi, J. M. Millam, M. Klene, C. Adamo, R. Cammi, J. W. Ochterski, R. L. Martin, K. Morokuma, O. Farkas, J. B. Foresman, D. J. Fox, *Gaussian 16, Revision C.01*, Gaussian, Inc., Wallingford CT 2016.
- [48] T. Lu, F. Chen, *J. Comput. Chem.* **2012**, *33*, 580.
- [49] R. D. Dennington, T. A. Keith, J. M. Millam, *GaussView 5.0.8*, Gaussian 2008.
- [50] P. Sharma, D. Damien, D. K. Nagarajan, M. M. Shajumon, M. Hariharan, *J. Phys. Chem. Lett.* **2013**, *4*, 3192–3197.
- [51] R. K. Dubey, N. Westerveld, F. C. Grozema, E. J. R. Sudhölter, W. F. Jager, *Org. Lett.* **2015**, *17*, 1882–1885.

Manuscript received: March 16, 2023
Revised manuscript received: March 24, 2023
Version of record online: April 21, 2023